

# Mapping the subcellular mechanical properties of live cells in tissues with fluorescence emission–Brillouin imaging

Kareem Elsayad,<sup>1\*†</sup> Stephanie Werner,<sup>2\*‡</sup> Marçal Gallemí,<sup>2§</sup> Jixiang Kong,<sup>2</sup> Edmundo R. Sánchez Guajardo,<sup>1</sup> Lijuan Zhang,<sup>1</sup> Yvon Jaillais,<sup>3</sup> Thomas Greb,<sup>2¶</sup> Youssef Belkhadir<sup>2\*†</sup>

Extracellular matrices (ECMs) are central to the advent of multicellular life, and their mechanical properties are modulated by and impinge on intracellular signaling pathways that regulate vital cellular functions. High spatial-resolution mapping of mechanical properties in live cells is, however, extremely challenging. Thus, our understanding of how signaling pathways process physiological signals to generate appropriate mechanical responses is limited. We introduce fluorescence emission–Brillouin scattering imaging (FBI), a method for the parallel and all-optical measurements of mechanical properties and fluorescence at the submicrometer scale in living organisms. Using FBI, we showed that changes in cellular hydrostatic pressure and cytoplasm viscoelasticity modulate the mechanical signatures of plant ECMs. We further established that the measured “stiffness” of plant ECMs is symmetrically patterned in hypocotyl cells undergoing directional growth. Finally, application of this method to *Arabidopsis thaliana* with photoreceptor mutants revealed that red and far-red light signals are essential modulators of ECM viscoelasticity. By mapping the viscoelastic signatures of a complex ECM, we provide proof of principle for the organism-wide applicability of FBI for measuring the mechanical outputs of intracellular signaling pathways. As such, our work has implications for investigations of mechanosignaling pathways and developmental biology.

## INTRODUCTION

Extracellular matrices (ECMs) of both plants and metazoans ensure the coherence of organ growth by enabling neighboring cells to physically assemble and communicate (1, 2). The ECM is a highly versatile structure that enables cells to acquire shapes that are adapted to the functional requirements of either soft or hard tissues, such as the brain or bones, respectively. The plasticity of the ECM in animals is regulated by the adhesive and structural functions of both glycosaminoglycans and fibrous proteins, such as collagen (1). In plants, ECMs have evolved into specialized molecular structures formed by a network of load-bearing stiff cellulose polymers sheltered in a matrix of structural, as well as signaling, glycoproteins (3, 4). Animal and plant cells both degrade and reassemble the constituent polymers of their ECMs to alter their stiffness and adapt to changes in hydrostatic pressure (1, 5). Thus, adaptation to fluctuating mechanical signals necessitates active regulation of the mechanical properties of the ECM. Conversely, changes in the mechanical properties of the ECM produce contextual signals that are integrated into transcriptional responses by signaling pathways that often originate at the cell surface (6). For ex-

ample, integrins in mammals and receptor kinases in plants convey mechanical signals to intracellular compartments for optimal cellular adaptation to the environment (4, 6).

Understanding how this complex biochemical and mechanical nexus operates to elicit adapted structural changes in the ECM is thus fundamental to fully grasp processes such as cell proliferation, migration, and differentiation (2). However, relating the mechanical and hydraulic contributions of cell compartments to live tissue behavior is challenging, because relevant quantitative biophysical parameters are difficult to obtain noninvasively at the subcellular scale.

Most of our current understanding of the ECM's mechanical responses is based on low-frequency perturbation-deformation measurements (7–13). These methods provide key information on the mechanical properties of the ECM; however, they are also typically limited to measurements near accessible surfaces and thus unsuitable for noninvasive three-dimensional (3D) studies. All-optical techniques can partly overcome the limitations of contact-based approaches (10, 13, 14); however, by design, these are often restricted to measurements at discrete positions. Methods that rely on acousto-optic interaction of light with inherent or induced density fluctuations are well suited for mapping mechanical properties in two or three dimensions (15–20).

Among other methods, spontaneous Brillouin light-scattering microscopy (17, 21, 22) is conducive to studying biological samples under desirable imaging conditions (18, 19, 23–33). The technique relies on the interaction of light with inherent thermal vibrations (acoustic phonons) in the sample (note S1) (17). When probing a sample with a single-frequency laser source, this interaction will result in a small component of the backscattered light that is spectrally shifted by several gigahertz relative to the wavelength of the probing laser. This spectral shift is referred to as the Brillouin frequency shift (BFS) and is proportional to the speed  $V$  of sound waves in the

<sup>1</sup>Advanced Microscopy Facility, Vienna Biocenter Core Facilities, A-1030 Vienna, Austria. <sup>2</sup>Gregor Mendel Institute, Austrian Academy of Sciences, Vienna Biocenter, A-1030 Vienna, Austria. <sup>3</sup>Laboratoire Reproduction et Développement des Plantes, Univ Lyon, ENS de Lyon, UCB Lyon 1, CNRS, INRA, F-69342 Lyon, France.

\*These authors contributed equally to this work (joint first authors).

†Corresponding author. Email: kareem.elsayad@vbcf.ac.at (K.E.); youssef.belkhadir@gmi.oeaw.ac.at (Y.B.)

‡Present address: Department of Forest Botany and Tree Physiology, University of Göttingen, 37077 Göttingen, Germany.

§Present address: Institute of Science and Technology Austria, 3400 Klosterneuburg, Austria.

¶Present address: Center for Organismal Studies, Heidelberg University, 69120 Heidelberg, Germany.

sample.  $V$  depends on and can be used to calculate the longitudinal elastic storage modulus  $M'$  at the probed region,  $V = \sqrt{(M' \rho^{-1})}$ , where  $\rho$  is the sample density.

The longitudinal elastic storage modulus ( $M'$ ), which is obtained using Brillouin light-scattering microscopy, and the Young's (or tensile) modulus ( $E$ ) are different. Young's modulus is measured in conventional stress-strain tests or perturbation-based techniques, such as atomic force microscopy (AFM). Both  $M'$  and  $E$  share the same units and are defined as the ratio of the applied pressure (stress) to the relative change in length (strain). However,  $M'$  assumes there are no deformations other than in the probing direction, and  $E$  allows deformations in directions other than the probing direction (21).  $E$  is a measure of the "stiffness" of a sample that can expand perpendicular to the perturbation direction, whereas  $M'$  assumes that the sample can only move in the direction of the probe and is thus generally larger (21).  $M'$  is also closely related to the bulk modulus ( $K$ ), which is a measure of the compressibility of a material and defined as the ratio of a stress-pressure applied from all directions to the resulting relative change in volume (21). Thus, for highly incompressible materials,  $M'$  and  $K$  will be almost equivalent, whereas  $M' > K$  for compressible materials (21).  $E$  of water is essentially zero, because it is a fluid; however,  $K$  and  $M'$  of water are relatively large due to its low compressibility. Thus, in hydrated tissue, Brillouin scattering will contain a distinct scattering contribution resulting from water ( $M' \sim 2.2$  GPa). This will produce a scattering peak at a defined frequency (in our case, 7.5 GHz), which needs to be systematically accounted for in the analysis.

Although, over an albeit limited range, Brillouin measurements of  $M'$  have been experimentally correlated with  $E$  measurements using AFM (18), the two measurements yield distinct results that cannot be compared without additional material information, because they measure moduli that consider the compressibility and incompressibility of the materials to different degrees and do so in different frequency regimes. Consequently, Brillouin light-scattering measurements result in higher moduli than AFM measurements.

For simplicity, we refer to the material property pertaining to the value of  $M'$  (as measured by Brillouin light-scattering microscopy) as stiffness, with a "stiffer" material being one with a larger value for  $M'$ , which typically corresponds to a larger BFS. Note, however, that this terminology is not universal in the literature where stiffness often also refers to the magnitude of other elastic moduli.

Brillouin light-scattering microscopy is efficient at noninvasively measuring the 3D mechanical properties of isolated cells (18). However, its implementation for high-resolution spatial mapping of live multicellular tissues, where it is challenging to designate stiffness to specific constituent components, has not yet been demonstrated. To overcome these limitations, we built a correlative fluorescence emission-Brillouin scattering imaging (FBi) microscope, which enabled the accurate assignment of mechanical properties to fluorescently labeled cellular structures. We showed that FBi measures the stiffness of plant ECMs and the plant cell cytoplasm at submicrometer resolution in 3D. With this approach, we demonstrated that changes in cellular hydrostatic pressure affect the stiffness of plant ECMs. We also established that the stiffness in the ECMs of elongating hypocotyls is symmetrically patterned with respect to the growth direction. This technique enabled the mechanical mapping of root ECMs, a plant organ that has so far not been amenable to perturbation-deformation methods due to its fragility. Finally, we showed that light-stimulated photoreceptor signaling maintains the stiffness of the hypocotyl cell ECM. On the basis of these results, we propose that FBi offers a gateway to start understanding how hydraulic and mechanical forces support

cellular functions while intersecting, synergistically or antagonistically, with signaling pathway activities.

## RESULTS

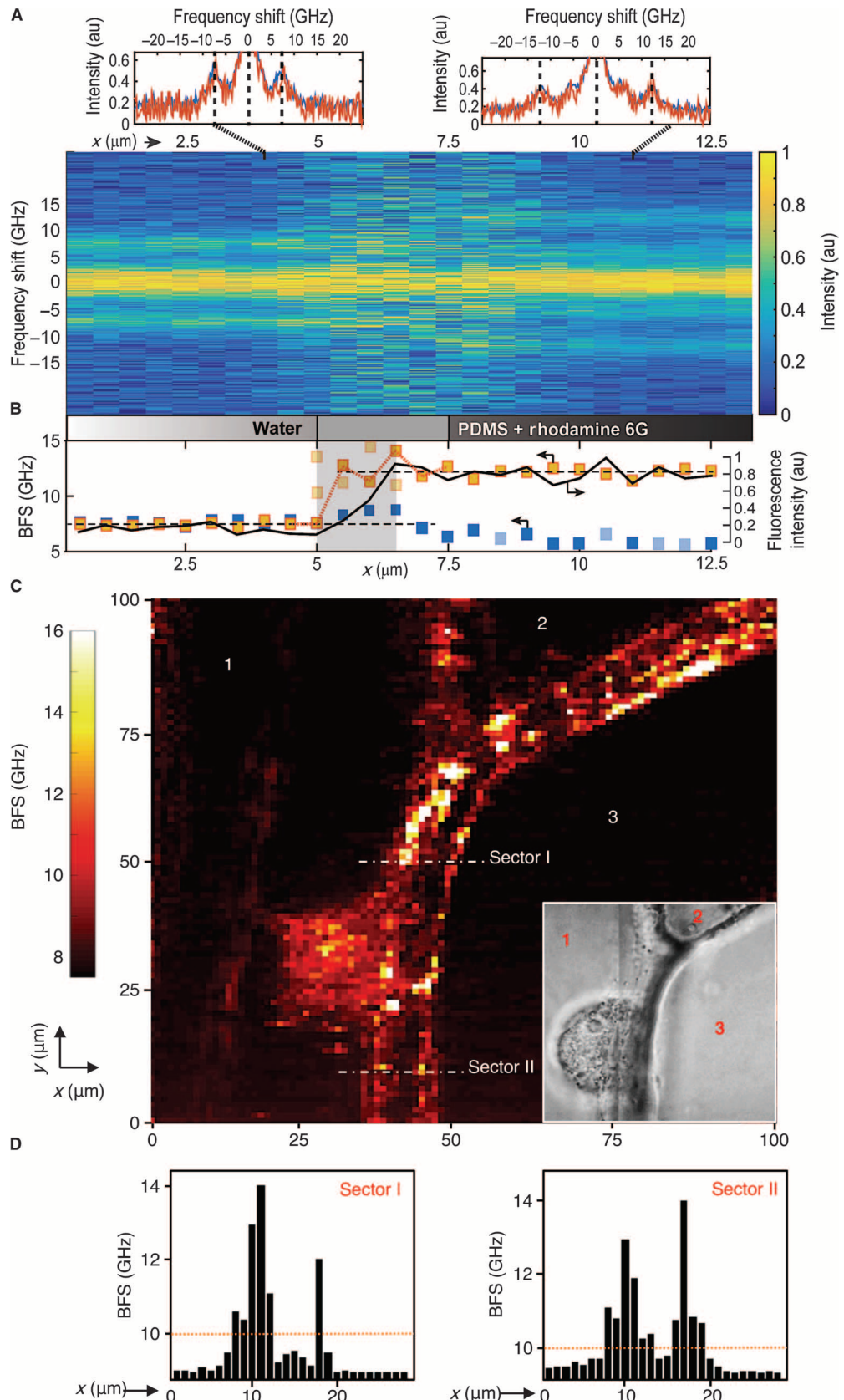
### Brillouin imaging maps the stiffness of plant ECMs at submicrometer-scale resolution

Here, we aimed to use Brillouin imaging in conjunction with fluorescence measurements to unambiguously assign the mechanical properties of the ECM in living plant cells. For this, we built a fluorescence-Brillouin light-scattering microscope with an excitation light (532-nm wavelength, single frequency) that is coupled into an inverted microscope frame and focused onto the sample with a high numerical aperture objective (NA, 1.3) (fig. S1). Backscattered light from the sample is focused through a pinhole and then spectrally separated: Wavelengths  $\sim 531$  to 533 nm are passed to a custom-built virtually imaged phased array (VIPA) spectrometer for stiffness measurements, and wavelengths  $>533$  nm are focused onto a photomultiplier tube (PMT) for fluorescence emission measurements (fig. S2, A to C). Because of the small free spectral range (FSR) of the VIPA spectrometer, one of our key challenges in achieving optimal resolution was to isolate the inelastic Brillouin spectra from the residual fluorescence, stray light, and elastic scattering (19, 34). We isolated the Brillouin spectra with cross-dispersion and spatial masking (fig. S2, A to C). To calibrate our setup, we used polydimethylsiloxane (PDMS) blocks infused with the fluorescent dye rhodamine 6G (R6G). We performed 1D scans at the interface of water and PDMS-R6G to measure simultaneous changes in the BFS and fluorescence (Fig. 1, A and B). An increase in BFS and fluorescence was apparent as we translated the sample to image from the water to the stiffer PDMS-R6G block (Fig. 1, A and B). From the parallel fluorescence and BFS measurements, we generated correlative Brillouin-fluorescence maps for both imaging methods with a lateral resolution better than 1  $\mu\text{m}$  (Fig. 1A). Thus, we successfully merged fluorescence emission and Brillouin imaging in one integrated setup.

Next, we tested whether our experimental setup could spatially map the stiffness of plant ECMs with the Brillouin light-scattering channel. For this, we performed Brillouin scans on the surface of epidermal onion cells (*Allium cepa*), a commonly used reference tissue for mechanical measurements (9, 35). A 2D lateral scan ( $x$ - $y$ ) of a  $\sim 100 \times 100$ - $\mu\text{m}^2$  area, encompassing the borders of three adjacent cells (Fig. 1C, cells 1, 2, and 3) and an isolated nucleus (Fig. 1C, cell 1), revealed different BFS, indicating distinct values for the hypersonic velocity ( $V$ ) and longitudinal elastic storage moduli ( $M'$ ), at the different regions (Fig. 1C and notes S2 and S3).

We detected about a twofold increase in BFS over a  $\sim 10$ - $\mu\text{m}$  sector surrounding the borders of the three adjacent cells, compared to the BFS in the more central cytoplasmic areas (Fig. 1C). In contrast, we measured the ECM thickness to be only  $\sim 1$   $\mu\text{m}$  using conventional bright-field microscopy. To rule out that the laterally extended high-BFS regions surrounding the ECMs were not the results of "off-target" measurements due to prolonged scanning time or due to the 3D curvature of the cells, we performed a series of short control scans. For this, we imaged our sample in stepwise increments of 1  $\mu\text{m}$  over a  $\sim 25$ - $\mu\text{m}$  distance covering the interfaces between the ECM, the plasma membrane, and the cytoplasm (Fig. 1C, sectors I and II). Again, an increase in the BFS was apparent as we translated the sample to image from the cytoplasm over the plasma membrane and the ECM (Fig. 1D). We interpreted this increase in BFS to indicate that the intra- and extracellular areas in close vicinity of the cell borders display mechanical signatures typical of biomaterials of heightened stiffness; thus, our microscope can map these with high resolution. We postulated that the stiffness at intracellular areas in close vicinity of the cell borders is due to the

**Fig. 1. Brillouin imaging maps the viscoelasticity of plant ECMs at submicrometer resolution. (A)** Brillouin scattering spectra (vertical axis) as a function of position for a 1D characterization scan across a water-R6G-infused PDMS interface, showing the transition of the Brillouin scattering peaks from ~7.5 GHz in the water to ~12.5 GHz in the PDMS. Characteristic spectra at  $x = 4$  mm and  $x = 11$  mm (orange lines) along with the averaged spectra for  $x < 5$  mm and  $x > 8$  mm (blue lines) are shown on top. **(B)** Measured fluorescence (solid black line) and BFS (intense orange squares) as a function of distance. Intense orange and intense blue squares are dominant peaks. Light orange and light blue squares correspond to peaks with intensities  $< 50\%$  of the dominant peaks. The red dashed line connects the dominant BFS peaks at the water-PDMS interface. Black arrows indicate the direction of the relevant  $y$  axis. **(C)** 2D ( $xy$ ) BFS map at the surface of three neighboring epidermal onion cells. The numbers in the image and the corresponding phase contrast image (inset) indicate the three distinct cells. Data are representative of  $n > 3$  independent samples. The circular structure in the phase contrast image is a nucleus. **(D)** Plots of BFS as a function of distance across the borders of cells 1 and 3 at two locations (sectors I and II) as indicated in (C). au, arbitrary units.



organization of the cytoskeleton, whereas the ECM contributes to the stiffness on the extracellular side.

### Cellular hydrostatic pressure modulates the stiffness of both the cytoplasm and the ECM

In deeper parts of the epidermal layer, the ECM is subjected to physical constraints imposed by neighboring cells (36). We tested whether the increased stiffness adjacent to the cell membrane also occurs near cells deeper in the epidermal layer. Because the axial ( $z$ ) resolution of Brillouin microscopy can limit the ability to assign precise mechanical parameters to a specific cell compartment, we guided the BFS measurements by fluorescently labeling the plasma membrane and detecting this fluorescence. We stained the plasma membrane of onion cells with the styryl dye FM4-64 and performed cross-sectional ( $xz$  and  $yz$ ) FBi scans (Fig. 2, A and B, and fig. S3, A and B). We used the correlation between BFS and plasma membrane fluorescence intensity to assess the overall contribution of the ECM to regions of increased BFS. Areas of high fluorescence corresponding to the plasma membrane correlated with increased stiffness along the same  $z$  plane (Fig. 2C). However, regions of low fluorescence intensity corresponding to the cytoplasm adjacent to the plasma membrane also displayed high stiffness (Fig. 2C).

FM4-64 can rapidly diffuse to endocytic membrane compartments in the cytoplasm, which would result in a different interpretation of the correlation between fluorescence signals and BFS (37). To rule out the possibility that FM4-64 uptake confounded the interpretation, we constructed a stable transgenic *Arabidopsis* line expressing a red fluorescent plasma membrane marker under the control of the strong cauliflower mosaic virus (CaMV) 35S promoter (35S::Lti6-tdTomato) (fig. S4A). FBi scans of the epidermal cells of 35S::Lti6-tdTomato hypocotyls also showed increased BFS adjacent to the plasma membrane, even at areas of low fluorescence (Fig. 2, D to F, and fig. S4, B and C); however, fluorescence above background was not detected in FBi scans performed on non-labeled onion cells (fig. S3C) or nontransgenic *Arabidopsis* plants (fig. S4, D and E). The cumulative stiffness calculated by assigning cytoplasmic material to all low-fluorescence pixels distributed either within or at least 5  $\mu\text{m}$  apart from the plasma membrane indicated that the cytoplasmic region closer to the membrane is stiffer. We found that this region is confined to  $\sim 5 \mu\text{m}$  on each side of the cell borders in *Arabidopsis* hypocotyls (fig. S5, A to E). Thus, our FBi scans confirmed the existence of a region of enhanced stiffness extending beyond the apparent ECM in both onion and *Arabidopsis* epidermal cells deeper within the tissue.

Collectively, our experiments indicated that the  $M'$  for all cytoplasmic regions (as defined solely by low-fluorescence signal) exhibits a relatively smooth continuum of stiffness between the ECM and the central cytoplasm for both onion and *Arabidopsis* epidermal cells (Fig. 2, C and F). Therefore, we hypothesized that the internal turgor pressure could modulate the stiffness of cytosolic regions surrounding the plasma membrane. To test this hypothesis, we subjected the hypocotyls of Lti6-tdTomato transgenic *Arabidopsis* seedlings to a hypertonic solution containing 0.8 M mannitol (fig. S6A), which causes shrinkage of the cell (plasmolysis), and performed FBi scans. Within 10 min of plasmolysis, we observed a drop and a redistribution of the BFS over an area of  $\sim 1 \mu\text{m}$ , approximately corresponding to the ECMs (fig. S6, A and B). We interpret this as indicating

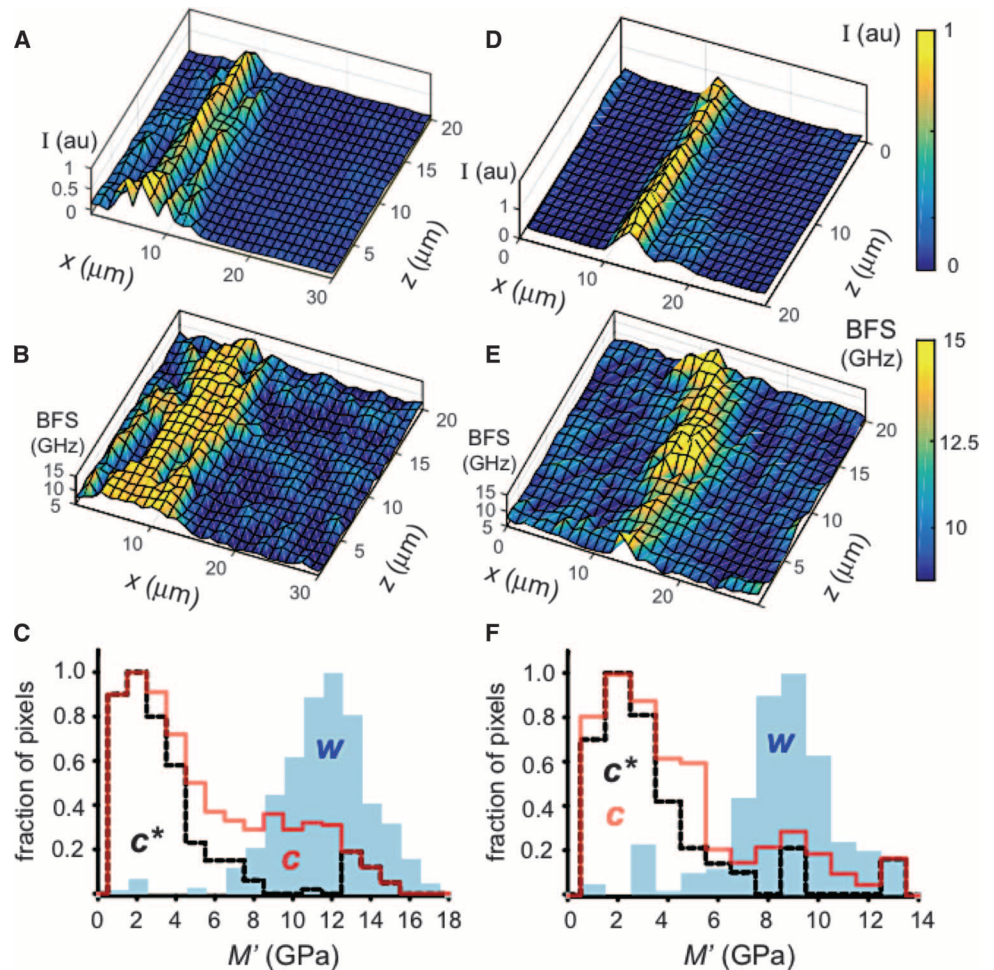


**Fig. 2. Cellular hydrostatic pressure modulates the stiffness of both the cytoplasm and the ECM.** (A and B) Representative cross-sectional ( $xz$ ) fluorescence intensity in arbitrary units and BFS (GHz) maps of ECMs of epidermal onion cells with membranes stained with the FM4-64 dye. (C) Longitudinal elastic storage modulus  $M'$  (GPa) obtained by assigning ECM material properties ( $n = 1.41$ ,  $r = 1.1 \text{ kg/m}^3$ ) to only high-fluorescence pixels ( $w$ , in light blue), cytoplasmic material properties ( $n = 1.38$ ,  $r = 1.0 \text{ kg/m}^3$ ) to all low-fluorescence pixels ( $c$ , in red), and cytoplasmic material properties to all pixels at least  $5 \mu\text{m}$  away from the plasma membrane ( $c^*$ , in black) as defined by peak fluorescence ( $n = 5$  cells). (D to F) Analogous to (A) to (C) but for 7-day-old *Arabidopsis* hypocotyl cells stably expressing the plasma membrane marker Lti6-tdTomato. Hypocotyls scans were all performed on longitudinal cell walls in the same sectors (cell number  $\sim 10$  starting from the root-hypocotyl junction). The data presented are representative of more than three independent experiments.

that the cytoplasm had lost its stiffness upon plasmolysis. In contrast, the fluorescence intensity was maintained, although it was distributed over a slightly larger area (fig. S6, D and E), consistent with the more diffuse Lti6-tdTomato fluorescent signal that we observed upon plasmolysis (fig. S4A). These results showed that FBI can be used to monitor the redistribution of stiffness in the ECM and cytoplasm of live cells in response to changes in hydrostatic pressure.

### Hypocotyls and root cells display distinct patterns of stiffness

The onion and *Arabidopsis* epidermal cells so far analyzed are relatively static in terms of their size and shape. To extend the application to a dynamic cell system, we analyzed epidermal cells in the elongation zones of hypocotyls and roots. These two cell types provide a framework for studying the mechanical constraints of directional growth, referred to as anisotropic expansion, because this tissue grows by the elongation of these cells, rather than their proliferation (38, 39). Thus, we measured the BFS of the long (parallel to the axis of growth) and short (perpendicular to the axis of growth) sides of the growing cells in the hypocotyls and roots of live *Arabidopsis* seedlings (Fig. 3, A and B). Our measurements imply that the ECM located on the long sides of hypocotyls cells is stiffer than the ECM on the short sides (Fig. 3, A and B). Additional 2D Brillouin ( $x$ - $y$ ) scans at a “three-way” cell junction in the hypocotyl also showed increased stiffness of the long-side ECM compared to the short-side counterparts (Fig. 3C). These scans also revealed the existence of a central connecting area of low stiffness that may accommodate the mechanical constraints exerted by simultaneously growing cells. To determine whether the differences in mechanical properties between the ECM of the long and short sides of hypocotyl cells are limited to the surface of the epidermis, we performed cross-sectional ( $y$ - $z$ ) scans at an ECM junction (Fig. 3D). The  $M'$  computed from the BFS measurements performed in the  $z$  axis indicated similar differences in stiffness between the long-side and short-side ECM in the inner parts of epidermal cells (Fig. 3D). To confirm that this difference represented a common property of the ECM of these elongating cells, we analyzed the stiffness of the ECMs in matching long and short sides of cells of independently grown hypocotyls and roots (Fig. 3, E and F). This revealed a significant difference in  $M'$  of the ECM of the long and short sides. In contrast, the elongating root cells had similar ECM stiffness on the long and short sides (Fig. 3B).

To control that our measurements can be interpreted as a difference in stiffness as opposed to a difference in the refractive index of the different ECMs, we exploited the fact that the fluorescence lifetime of fluorophores depends on the local refractive index (note S4) (40–45). For studying the variation in refractive index of the ECM along the long and short sides of *Arabidopsis* cells, we used a stable transgenic line expressing a plasma membrane-associated receptor tagged with a yellow fluorescent protein (BR11-mCitrine) (46, 47). For direct comparison with our Brillouin scattering measurements, we performed time-resolved confocal fluorescence lifetime on the outer cells of the hypocotyls (fig. S7, A to C). The average lifetime distribution indicated that, within experimental uncertainty, the average refractive index of the ECMs in the short (fig. S7, D and E) and long (fig. S7, F and G) sides of the cells were comparable to each other and thus cannot account for the observed variations in BFS. Additional time-resolved fluorescence lifetime measurements at the three-way cell junction further indicated no obvious differences in optical properties for both the long-side and short-side ECMs (fig. S7, H and I). Together, our results implied that the different stiffness contributions of the ECM located on the long sides of hypocotyl cells may promote anisotropic growth while avoiding anomalous transverse swelling.

### Epidermal and endodermal root cells display similar patterns of stiffness

The *Arabidopsis* root is typically composed of three radially symmetric cell layers that surround a central vascular system (Fig. 4A) (48). Our analysis of the ECMs of *Arabidopsis* root cells was so far performed on the outermost epidermal layer. Here, we extended our measurements to the more inner cortical and endodermal layers (Fig. 4A). We performed cross-sectional ( $x$ - $z$ ) Brillouin scans along the ECMs at the interface of the epidermal and cortical layers. With 2D Brillouin imaging scans, we visualized discrete points of high stiffness that seem to connect the root cells (fig. S8A). To acquire mechanical information on a whole root cross section, we also performed large-area cross-sectional ( $x$ - $z$ ) Brillouin imaging scans (fig. S8, B and C). The BFS maps from the large area scans again revealed that epidermal cells are connected through discrete points of high stiffness, which may correspond to regions of “merged” ECM. However, our Brillouin scans did not have sufficient spatial resolution to assign precise ECM mechanical parameters to a specific cell type.

Therefore, we performed unidirectional FBI depth ( $z$ ) scans on a transgenic *Arabidopsis* line (*CASPI1::mCherrySYP122*) expressing a plasma membrane marker that is specifically expressed in the root endodermis (Fig. 4A) (49). We monitored the BFS and plasma membrane fluorescence intensity to measure unambiguously the stiffness of the ECM in the endodermal cell layer (Fig. 4B). With FBI scans along the same  $z$  plane, we detected three areas of high stiffness, of which only one also had high fluorescence. FBI scans on wild-type plants further indicated that the observed relationship between fluorescence and BFS in the endodermal cells of the *CASPI1::mCherrySYP122* transgenic line is specific (fig. S9, A and B). Our instrument can map stiffness and fluorescence of the ECMs with high resolution deep within complex tissue environments.

### Red and far-red light signals modulate the stiffness of plant ECMs

Light signals are plant morphogens and regulate the development of plant organs in various ways. For example, light inhibits hypocotyl elongation (50, 51). Here, we used this light-dependent response to test our instrument. We analyzed the red and far-red light-insensitive photoreceptor double-mutant phytochrome A and B (*phyA phyB*), which fail to stop growth in response to light (50). Cross-sectional ( $x$ - $z$ ) Brillouin scans along the ECMs located on the long sides of rapidly elongating *phyA phyB* hypocotyl cells displayed significantly reduced stiffness ( $M' \sim 6.5$  GPa) compared to elongating hypocotyl cells in the wild-type plants ( $M' \sim 8.5$  GPa) (Fig. 5, A and B). Because the cytoplasm of both mutant and wild-type plants displayed similar stiffness, the results indicated that the reduced stiffness of the ECM in *phyA phyB* plants was not due to changes in cytoplasm viscoelasticity and was due to a change in the mechanical properties of the ECM (Fig. 5B). Because current paradigms propose that elongation growth is promoted by selective loosening of the ECM, we attribute the elongated phenotypes of *phyA phyB* hypocotyls to the lowered stiffness of their ECMs (39, 52, 53).

We also tested if the inhibition of cellulose biosynthesis, the main constituent molecule of the cell wall (and thus ECM) in plants, affected the stiffness of the ECM by transiently inhibiting cellulose synthesis with isoxaben, a benzamide compound that specifically blocks the activity of subunits in the cellulose synthase complex (54). We subjected wild-type and *phyA phyB* seedlings to isoxaben and monitored the stiffness of the ECM in the long sides of hypocotyls cells (Fig. 5C). Analysis of the variance in  $M'$  for the long walls in both untreated and isoxaben-treated wild-type samples showed that  $M'$  is significantly more broadly distributed in untreated samples, whereas the variance of  $M'$  was similar in untreated and treated *phyA phyB* mutants. We thus conclude that inhibition of cellulose synthesis by isoxaben promotes a tighter distribution with less variability in stiffness in the ECM or

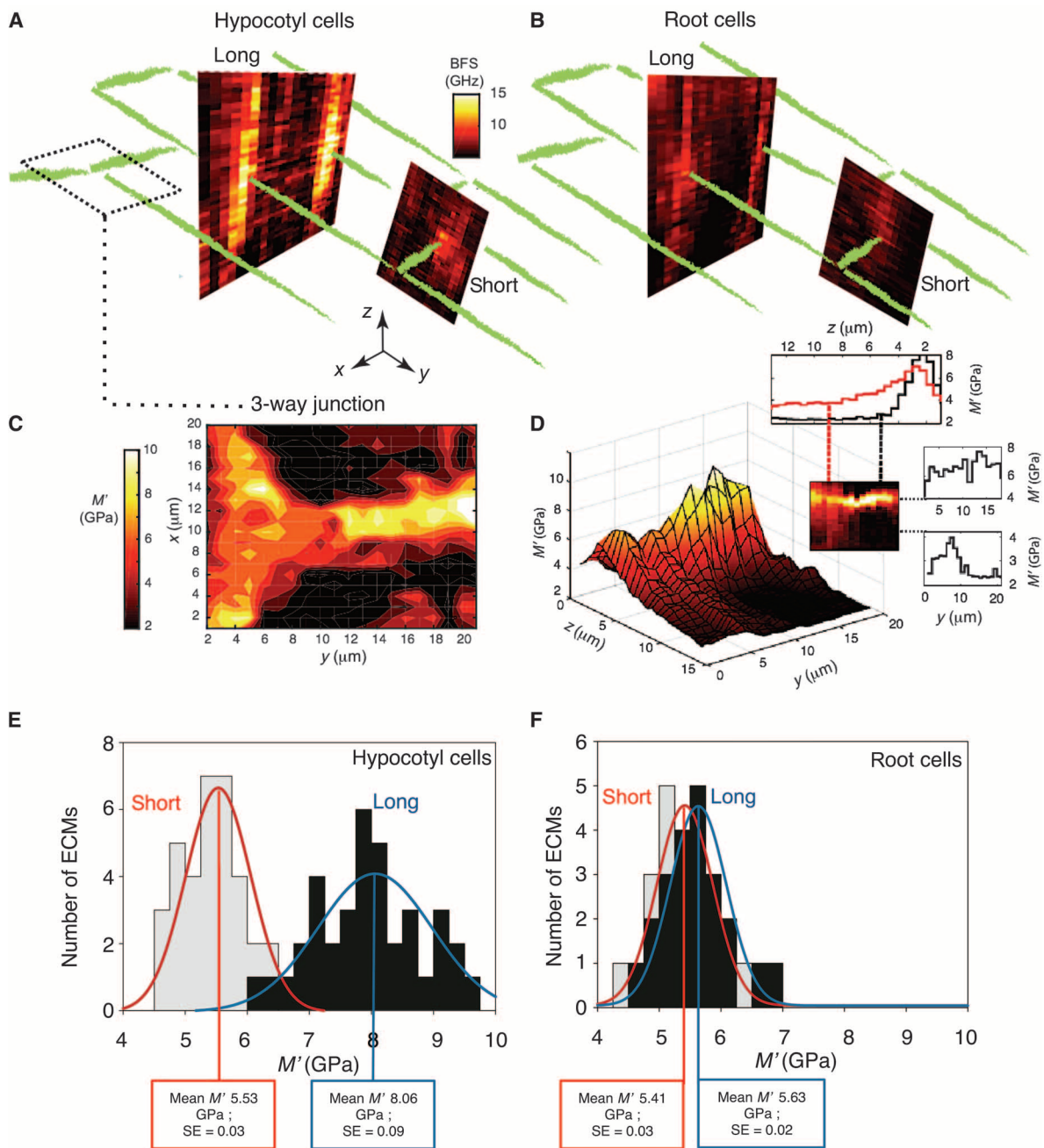


**Fig. 3. Hypocotyl and root cells display distinct patterns of stiffness.** (A and B) Representative cross-sectional ( $xz$  and  $yz$ ) BFS maps of ECMs along the long and short sides of elongating hypocotyl cells (A) or root cells (B) in a 7-day-old *Arabidopsis* plant. Image orientation is indicated with  $xyz$  key. (C) Representative in-plane  $xy$  maps of the longitudinal elastic storage modulus ( $M'$ ) at a three-way junction in epidermal hypocotyl cells. (D) Left: Representative cross-sectional  $yz$  maps of the longitudinal storage moduli ( $M'$ ) at a three-way junction in epidermal hypocotyl cells. Right: Longitudinal storage moduli ( $M'$ ) plots as a function of distance in the  $y$  plane and  $z$

plane ( $\mu\text{m}$ ) at the location of ECMs. (E) Cumulative plots of  $M'$  in the ECMs of long (black bars) and short (gray bars) sides of hypocotyl cells fitted with normal distributions (red and blue lines). Difference in mean  $M'$  of long and short walls is statistically significant at the level  $P < 0.01$  ( $n > 30$  cells). Mean  $M'$ , SE. (F) Same as in (E) but for roots. Difference in the mean of the long and short walls for the root of  $n = 10$  cells is not statistically significant. Hypocotyl scans were all performed on the walls belonging to the same cell sectors (cell number  $\sim 10$  starting from the root-hypocotyl junction).  $t$  test analysis was used to compare the mean  $M'$ .

the cytoplasm of wild-type plants. Because reduction in the cellulose content in the ECM could affect cell shape and, hence, function, we speculate that plant cells use cellulose-independent mechanisms to regulate the mechanical properties of their ECMs. These data also showed that the FBi method can be used to monitor the effects of chemicals that inhibit ECM biosynthesis and to study the mechanical outputs of light signaling pathways.

**DISCUSSION**

The mechanical properties of subcellular compartments play a major role in determining the shape of cells and entire organisms. However, understanding mechanical properties such as stiffness is not trivial and requires combining multiple measurement techniques. Our current understanding of the mechanical properties of ECMs in plants and animal cells is based on low-frequency perturbation-deformation measurements at the macroscopic through nanoscopic scales (7–13). In this frequency regime, a given volume of the ECM is perturbed at low enough repetition rates to allow nearly complete mechanical relaxation between probing cycles. By using such methods, one thus gains information on the low-frequency mechanical

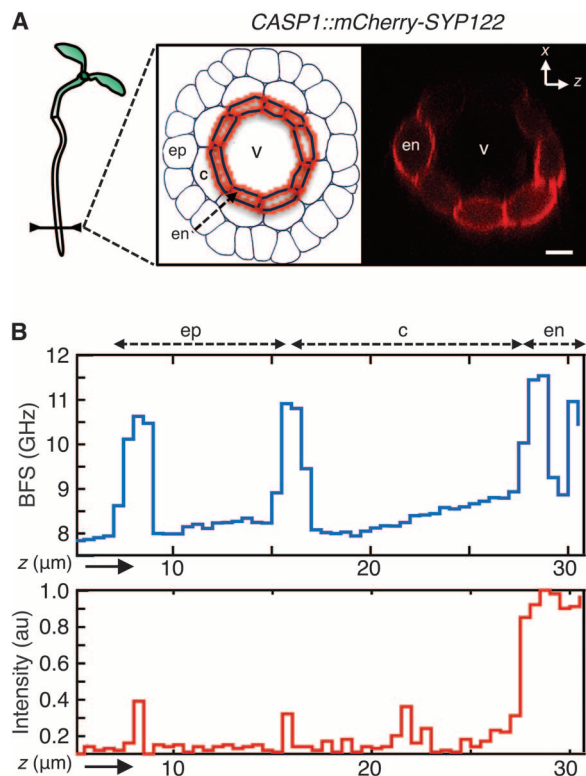


**Fig. 4. Epidermal and endodermal root cells display similar patterns of stiffness.** (A) Left: Depiction of an *Arabidopsis* seedling. Middle: Schematic of a root transversal section. Cells highlighted in red belong to the root endodermal layer. ep, epidermal cell layer; c, cortical cell layer; en, endodermal cell layer; v, vascular system. Right: Cross-sectional fluorescence image showing the endodermal-specific fluorescence signal at the plasma membrane of the endodermal cells in the marker line CASP1::mCherry-SYP122. Scale bar, 10 μm. (B) Results of cross-sectional FBi scans of root cells. BFS is shown in blue. Fluorescence intensity is shown in red. Representative data from more than three independent experiments.

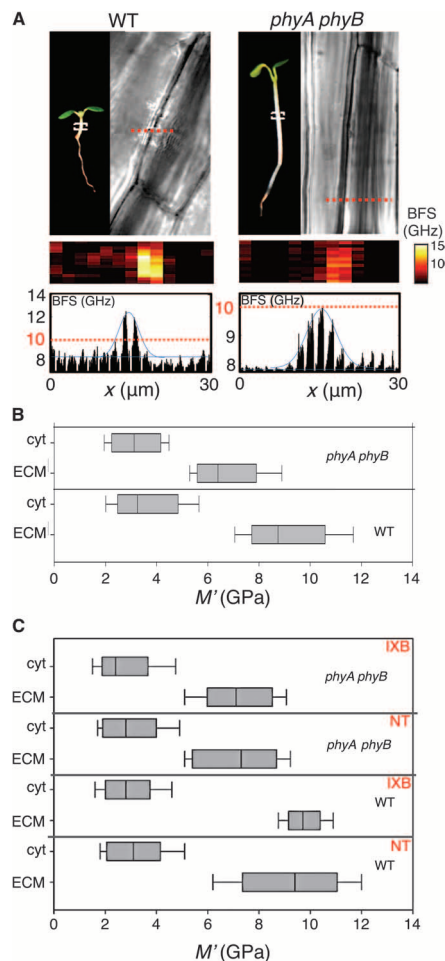


**Fig. 5. Red and far-red light signals modulate the stiffness of plant ECMs.** (A) Top: Representative pictures of wild-type (WT) and *phyA phyB* *Arabidopsis* seedlings (left); corresponding representative pictures of hypocotyl cells obtained by transmitted light microscopy (right). Middle: Cross-sectional representative BFS heat maps of ECMs of the long sides of hypocotyl cells of the respective genotypes. Bottom: Corresponding BFS plots as a function of scan distance (μm). Scanned sectors are indicated on top light images with dashed red lines. For clarity purposes, the scale of the y axis is different for the two genotypes, and for comparative purposes, a red dotted line indicates BFS = 10 GHz is drawn. (B) Quantification of the derived longitudinal elastic storage modulus  $M'$  (GPa) for the cytoplasm (cyt) and the longitudinal ECMs in the genotypes indicated on the left ( $n = 5$  for each). The difference in the mean value  $M'$  between WT and *phyA phyB* genotypes is significant ( $t$  test,  $P < 0.05$ ), whereas there was no significant difference in the variance at this level ( $f$  test,  $F = 2.32$ ). The cytoplasm also showed no significant difference in the mean or variance. (C) Quantification of the derived longitudinal storage modulus  $M'$  (GPa) of longitudinal hypocotyls ECMs after a 72-hour treatment with 10 μM isoxaben (IXB; in red) or 0.5× MS liquid medium (NT) ( $n = 9$  for each). Whereas there is no significant difference in the mean between the ECMs for treated and untreated WT cells, the variance differed significantly ( $F = 7.48$ ,  $P < 0.05$ ) but not for the treated and untreated *phyA phyB* mutants ( $F = 4.58$ ). Finally, there was no significant change in the mean or variance of  $M'$  in the cytoplasm between treated and untreated cells of both genotypes. All hypocotyls scans were performed on longitudinal cell walls in the same sectors (cell number ~10 starting from the root-hypocotyl junction).

properties of the ECM. Yet, these approaches give little information about cells deeper within tissues and often require a partial reduction in hydrostatic pressure to yield useful information. At higher probing frequencies (~GHz), the nature of the mechanical relaxation mechanism will contribute to the overall mechanical response. Consequently, materials typically appear orders of magnitude stiffer in this regime (19, 20). Accordingly, the calculated  $M'$  obtained by BFS measurements of onion ECMs is much larger than the reported Young's modulus ( $E = 80$  MPa) obtained using standard perturbation-deformation measurements (55) but comparable in magnitude to measurements performed using picosecond acoustics (15).

Optical techniques, such as spatial-temporal fluctuation measurements and molecular rotational mobility analysis, have been used to acquire biomechanical parameters in the low- and intermediate-frequency regimes (10, 13). Optical label-free inelastic scattering techniques, such as picosecond ultrasonics and Brillouin microspectroscopy, have been used to map the viscoelasticity of different subcellular compartments in the high-frequency regimes (18, 23, 56). Brillouin scattering microscopy was believed to be limited by the use of low-NA lenses, which can affect the spatial resolution in the lateral direction and in the  $z$  plane. As such, accurate Brillouin 3D maps in complex biological environments were difficult to obtain. Here, we demonstrate 3D correlated FBi for investigating the mechanical properties of subcellular compartments at high resolution in complex plant tissues. With the subcellular resolving power of our instrument, we measured the stiffness of plant ECMs at high resolution and overcame existing depth-imaging limitations.

Brillouin scattering imaging is a technology still in development; we expect further improvements in aspects such as light efficiency, stray light rejection, and non-scanning high-resolution spectral measurements with next-generation VIPA-based setups (19, 20, 34). Brillouin imaging is often championed as a completely label-free approach, which is desirable for many biomedical applications. This can, however, at the same time serve as its Achilles' heel, because it cannot definitively assign mechanical properties to different cellular regions. This is especially true in basic biomedical research where one is often interested in the quantitative correlation of the mechanical properties to the abundance of a specific chemical constituent or morphological feature, as would be essential for studying mechanical responses driven by signaling pathways. Over the past several decades, fluorescence microscopy has been the tool of choice for molecular biology because of its molecular specificity and typically high signal-to-noise ratio even within deeper tissues. We expect that the ability to generate high-resolution parallel and pixel-wise correlated high-frequency viscoelasticity and fluorescence maps will be a welcome addition to the microscope toolbox. We propose that FBi should be added to the current arsenal of methods routinely used to investigate the signaling aspects of cellular tethering in growing tissues (8, 11, 35).

The importance of turgor pressure in regulating mechanical responses in animal and plant cells is well established (5, 57–61). Using pixel-wise correlative analysis of fluorescence and stiffness, we showed that the plant cell cytoplasm itself is stiffer in the immediate vicinity of the plasma membrane under turgor pressure, which is consistent with results from force-based studies reporting an effectively stiffer ECM under turgor pressure (36, 61). Our results with the effects of plasmolysis showed that the cytoplasm can modify the stiffness  $M'$  of the ECM in a manner dependent on the degree that it is compressed by the vacuole. We posit that a full understanding of mechanotransduction events in the context of ECM homeostasis requires a model that accounts for the spatially dependent cytoplasm stiffness near the cell borders.

Together with the internal turgor pressure, the extent to which the ECM changes its shape under tensile pressure will promote the rate of cellular

expansion in plants (59, 62, 63). The *Arabidopsis* hypocotyl is a model system for studying cell elongation, because growth in this organ occurs with almost no contribution from cell division (39). By FBi, we found that the ECMs located parallel to the growth axis of *Arabidopsis* hypocotyls displayed enhanced stiffness signatures compared to the ECMs located perpendicular to the growth axis. This distribution of stiffness could help plants avoid anomalous transverse swelling and promote anisotropic growth (60, 62, 63). Our results diverge from other findings in which low-frequency AFM stiffness measurements indicate that the ECMs along the shorter side (perpendicular to the growth axis) are stiffer than their longitudinal counterparts in plasmolyzed cells of dark-grown hypocotyls (64). Not only were the growth conditions different than the ones we used, but AFM measurements probe the low-frequency elasticity (FBi probes high-frequency elasticity) and frequency-dependent properties of the longitudinal and transverse ECMs may be distinct. However, a direct comparison between AFM and Brillouin scattering measurements is not possible because of the differences in the elastic moduli that they detect. We consider it also likely that the differences in stiffness distribution between the results of Peaucelle *et al.* (64) and our results arise from the lack of light and difference in hydrostatic pressure under which the two sets of experiments were performed.

Our study with the photoreceptor mutant *phyA phyB* revealed that the ECMs of the long sides of cells that are insensitive to red and far-red light signals display significantly reduced  $M'$  compared to the same cells in wild-type plants. These results indicated that plant phytochromes, which function as transcriptional regulators in the nucleus, activate pathways that redefine the mechanical parameters of the ECMs to modulate elongation growth. Our assays with the cellulose biosynthesis inhibitor isoxaben showed that reduced production of this critical cell wall component promotes a spatial redistribution of  $M'$  in the ECM vicinity for wild-type plants, without a significant change in the average stiffness of the ECM. Because a decrease in cellulose synthesis can be compensated by an increase in synthesis of stiff lignin polymers (65), we speculate that isoxaben-treated wild-type plants may increase lignin deposition in the ECM to maintain stiffness. The insensitivity of *phyA phyB* plants to the chemical may indicate that red or far-red light signals regulate lignin synthesis and deposition in the ECM. This finding will guide further investigations aimed at understanding how light signaling pathways impinge on the synthesis of structural constituents of plant ECMs. Overall, our data reinforced the model that synthesis and deposition of structural molecules in plant ECMs are subject to feedback mechanisms that may link stiffness to the rate of cell elongation (53). To conclude, we have demonstrated the application of Brillouin microscopy in conjunction with genetics and chemical treatment approaches to measure the mechanical outputs of red and far-red light signaling pathways *in vivo*.

The study of mechanical transduction in live cells requires a better understanding of how intracellular signaling pathways enable cells to generate an adapted mechanical response. Conversely, understanding how ECM stiffness can modulate the outputs of key developmental or immunity-related signaling pathways is critical to understand how the mechanical properties of a given tissue influence both the body plan of an organism and its ability to defend itself against pathogens. Approaches and methodologies to investigate these questions partly rely on novel conceptual frameworks driven by advances in biophysical technologies. Our work explores the tractability of a new method that holds promise for bolstering emerging studies in the field of mechanotransduction. Because of its speed and simplicity in acquiring, analyzing, and correlating fluorescence and high-frequency viscoelasticity data, we envision that FBi could be useful in a broad range of applications, including measuring mechanical responses in conjunction with fluorescently labeled osmo- or mechanoreceptors and in

mutant screens with chemical treatments in conjunction with fluorescent markers.

## MATERIALS AND METHODS

### Spatial resolution calibration measurements

PDMS–rhodamine G blocks were made on high-precision glass coverslips using PDMS/Sylgard 184 (ratio 9:1) (Dow Corning) mixed with varying amounts of rhodamine G. Curing was performed for 2 hours at 65°C. A ~3-mm hole was first punched in the center of the blocks and then filled with distilled water. Closed-loop single-axis piezo scans were performed across the PDMS water interface in 500-nm increments, with a laser power of ~2 mW at the sample. The apparent resolution is larger than the diffraction-limited resolution one would expect for the objective for several reasons: (i) The rhodamine concentration was significantly lower toward the edge of the PDMS block likely due to diffusion into the water where some residual fluorescence was observed, and (ii) the low spatial sampling (500 nm) meant that higher-resolution features could by design not be resolved.

### Sample scanning

Images were acquired by scanning the sample. Samples were mounted on a custom holder fixed to a long-range (340- $\mu$ m travel range) three-axis piezo stage (E-710, Physik Instrumente). The piezo stage was fixed on top of a servo-motor stage (MS-2000 XYZ, Applied Scientific Instruments), which was mounted on the microscope frame. The sample was raster-scanned (closed loop) with the piezo in increments typically between 300 and 500 nm. The acquisition (dwell) time at each position was between 1 and 4 s for most samples studied, such that a 30  $\times$  30–pixel map could be generated in ~30 to 45 min. Faster measurements could be performed at compromised spectral resolution by binning pixels on the electron-multiplying charge-coupled device (EMCCD) or compromising spectral fit accuracy. The measured laser power after the objective at the sample was always between 1 and 5 mW (typically ~3 mW). These intensities showed no adverse effects on the samples for several hours after acquisition, and plants were observed to continue to develop normally after completion of our measurements.

### Onion preparation and imaging

Common onion (*A. cepa*) was obtained from a local grocery store. For microscopy, epidermal peels from the adaxial side of the third or fourth onion scale were used. The peels were around 0.5 cm in diameter. Epidermal peels were mounted on a glass slide in a drop of water, with the ECM side facing the coverslip. For FBi measurements, FM4-64 was used in a final concentration of 5  $\mu$ g/ml dissolved in H<sub>2</sub>O. Onion peels were incubated in this solution for 90 min and then transferred to a glass slide with a drop of water immediately before imaging.

### *Arabidopsis* preparation and imaging

*Arabidopsis* seeds were sown in 0.5 $\times$  MS agar medium (pH 5.7) containing 1% (w/v) sucrose and 0.8% (w/v) agar (Duchefa Biochemie) and kept at 4°C for 72 hours in the dark for seed stratification. Thereafter, seeds were grown for 7 days in a growth chamber constantly kept at 21°C and a 16-hour-light/8-hour-dark cycle. For hypocotyl analysis, the 9-11th cell was imaged consistently by counting the epidermal cells starting from the root-hypocotyl junction. Cells on the elongation zone were chosen for root measurements. Seedlings were mounted on glass slides and covered with an agar pad immediately before imaging. For plasmolysis experiments, Lti6-tdTomato seedlings were grown as described above and were subjected to either water (control) or 0.8 M mannitol treatment for 10 min. Wild-type

and *phyA phyB* seedlings were grown and imaged in the same manner as described above. For cellulose synthesis inhibition assays, *Arabidopsis* seedlings grown on plates were subjected to 10  $\mu$ M isoxaben treatments in liquid 0.5 $\times$  MS medium for roughly 72 hours before imaging.

### Microscope setup

Excitation was achieved with a continuous-wave actively locked single-frequency diode laser (532 nm, 750 mW; Torus, Laser Quantum). Before coupling into the main optical setup, the beam was passed through a Faraday rotator/isolator (IO-5-532-HP, Thorlabs) to attenuate side bands and a Keplerian telescope with a pinhole at the focus to assure perfect collimation and expand the beam. Polarization and attenuation of the lasers were controlled with a subsequent half-wave plate and a polarizing filter. The collimated beam was coupled into the optical setup through a nonpolarizing 90:10 (T:R) beam splitter. The light transmitted through the beam splitter was used to measure the laser power and stability using a scanning Fabry-Perot interferometer between sample measurements and was blocked during sample measurement. The transmitted light was also used for calibration measurements (typically on water, ethyl alcohol, and glycerol) that were taken between sample measurements. The incident laser light reflected from the beam splitter was coupled into the lower right port of an inverted microscope frame (IX73, Olympus), where the tube lens had been removed and focused onto the sample by the objective lens. For most of our scans, and unless otherwise specified, we used a high-NA objective (Olympus UPlanSApo 1.3 NA, 60 $\times$  silicone oil immersion). An iris immediately before coupling into the microscope frame was used to adjust the effective excitation and detection NA. Because there is an angular dependence to the BFS that results in spectral broadening for finite NA measurements (20), we limited our effective NA to ~0.9 (as determined by measuring the lateral full width at half maximum of the point spread function of subdiffraction limit TetraSpeck fluorescence beads). The observed spectral broadening did not prove detrimental to fitting of the BFS, although we did use “broadened” Lorentzians (Voigt functions) for our Brillouin peak fits.

### Wide-field imaging

Epi-illumination for wide-field fluorescence images of the probed sample region was obtained by inserting a (long-pass) dichroic filter set into the carousel in the upper deck of the microscope frame through which we coupled a halogen lamp from the back port of the microscope frame with a condenser for epi-illumination. Alternatively, a transmitted light or differential interference contrast (DIC) image could be obtained by illuminating the sample from the condenser arm of the microscope and, for DIC images, inserting the appropriate Wollaston prisms and polarizers. Wide-field detection was possible by switching the out-coupling mirror in the lower deck with a (long-pass) dichroic mirror and then projecting the long wavelength image onto a CCD camera (1500M-GE, Thorlabs) mounted on the lower left port of the microscope frame with a  $f = 180$  mm achromatic tube lens.

### Confocal detection

The backscattered light that was coupled out through the lower right port of the microscope was first focused through a 100- $\mu$ m pinhole and collimated to have a beam diameter of ~2 mm. This was subsequently split with a dichroic mirror (LPD02-532RU-25, Semrock) for fluorescence imaging, Brillouin scattering measurements, or both.

### Fluorescence

The long wavelength–transmitted light was passed through a band-pass filter chosen to cover the emission spectrum of the desired fluorophore (for example, FF02-641/75-25, Semrock) before being focused onto a PMT (PMM02, Thorlabs) with a  $f = 150$  mm achromat. The PMT gain voltage

was controlled manually, and the amplified photon count was read out with a USB DAQ module (DT 9834-16-4-16-BNC, Data Translation) connected to a PC running a MATLAB (MathWorks) routine. The PMT readout was synced to the movement of the stage and the exposure time of the Brillouin spectrometer EMCCD camera (ImagEM II, Hamamatsu). The EMCCD acquisition start time for each scanning point was programmed to lag the respective PMT acquisition start time by a software-adjustable amount, which was typically set to 0 to 1 s depending on the sample. This allowed for the probed region to be partially bleached before collection of the Brillouin spectra to obtain cleaner spectra at each point.

### Spectrometer

Light was first passed through a 2-nm band-pass filter (LL01-532-12.5, Semrock), which was tilted to optimize transmission at the laser wavelength and remove longer wavelength, stray, or fluorescence light, followed by a polarizer aligned with its axis parallel to the probe beam polarization. The signal was then focused into the opening window of the VIPA, tilted vertically at  $2^\circ$  ( $\pm 0.5^\circ$ ) relative to the optical axis (as measured from the displacement of back-reflected light relative to the optical axis), with a ( $f=200$  mm) cylindrical lens. For FBI measurements and measurements for which background fluorescence was a problem, a set of large N-SF11 Equilateral Dispersive Prisms (Thorlabs) was placed in a cross-dispersion configuration (perpendicular to the VIPA tilt axis and optical axis) after the VIPA. Before being incident on the prisms, the beam was expanded in the direction parallel to the VIPA dispersion axis to cover a larger area of the prism. Residual inelastic scattering and stray light could thereby be dispersed perpendicular to the main optical and VIPA spectral axis. The angle of the two prisms was aligned, such that the angular-spectral divergence of light leaving the prisms in the cross-dispersion axis was maximized. Unlike with an echelle spectrometer (66) or the cross-dispersion double VIPA design (19), the cross dispersion was not always sufficient in our implementation to cleanly separate many spectral orders (that is, comparable to spectral bandwidth of VIPA spectrometer) but proved sufficient for the current purpose. The advantage of using prisms (despite the lower dispersive properties and spectral resolution compared to gratings and VIPAs) is that one does not have the issue of orders “folding over” (being superimposed), which would result in overlaps of the measured spectrum. A 2-inch achromatic lens was used to project the VIPA and prism-dispersed spectrum onto an image plane, which was subsequently imaged on the EMCCD camera with a magnification of  $\sim 12$ . A spatial mask (a 3-mm-diameter EM 1D grid) was carefully positioned with a manual translation stage in the intermediate image plane to suppress the Rayleigh scattering peak when it became problematic in opaque samples. Our custom-designed VIPA (manufactured by SLS Optics) had a measured FSR of  $\sim 33$  GHz and a finesse of 60 to 70. It consisted of a 3-mm-thick fused quartz slide ( $n=1.460$ ) and reflective dielectric coatings on both the input and the exit face ( $R=95.0\%$  and  $>99.7\%$  at 532 nm, respectively), with the exception of a small 532-nm antireflective-coated window on the input face. The analyzed signal was focused into this opening with a cylindrical lens ( $f=200$  mm). For nonfluorescence measurements, either a double or single VIPA configuration without a prism was used. These closely resembled the design described in (19, 67) with the exception of using a single spatial mask in a final intermediate image plane, which was imaged on the EMCCD chip with an increased magnification ( $\sim 12\times$ ) to isolate regions of interest in the spectral image.

### Software and acquisition control

All hardware control and real-time analysis were performed using a custom-written MATLAB (MathWorks) script, through which control of all scanning and acquisition parameters were also possible from a graphics user interface.

### Spectral analysis

The spectra projected on the EMCCD were first scaled to yield the intensity as a function of frequency. The scaling function was obtained by performing calculations of the spatial dispersion in the paraxial regime. The validity of this was checked before each imaging session and optical realignment by noting the spacing between the different orders of the Rayleigh scattered peaks and measuring test samples (typically water, ethyl alcohol, and glycerol). For both the Stokes and anti-Stokes Brillouin peaks, Voigt functions were typically used for fitting, because they provided slightly better fits than pure Lorentzians, which was likely due to the spectral broadening resulting from the finite NA, and other low-energy scattering processes in the sample. Fitting was performed using a custom-written MATLAB script, which first removed stray light contributions and background noise, aligned and projected the spectral axis imaged on the camera chip, rescaled this projection by an experimentally verified extrapolated dispersion function, and called a peakfit function of MATLAB (MathWorks) to perform linear least-squares fitting of the peaks. The  $M'$  in the backscattering geometry was calculated as  $M' = \lambda^2 \omega_B^2 \rho / (2n)^2$ , where  $\lambda$  is the probing wavelength,  $\omega_B$  is the fitted BFS, and  $\rho$  and  $n$  are the density and refractive index taken from the literature. For the cytoplasm, the values used for calculating  $M'$  were  $n=1.35$ ,  $\rho=1000$  kg/m<sup>3</sup>, and for the ECM, they were  $n=1.41$ ,  $\rho=1100$  kg/m<sup>3</sup> (68).

### Spectral calibration

Calibration studies were performed on three types of test samples: ethyl alcohol, water, and glycerol. The obtained  $M'$  values were 0.95 ( $\pm 0.08$ ), 2.20 ( $\pm 0.15$ ), and 4.16 ( $\pm 0.20$ ) GPa, respectively, in agreement with previously documented values (1.0, 2.1, and 4.3 GPa, respectively, at ambient temperatures). In each case, a drop of the respective liquid was pipetted onto a high-precision coverslip, the objective was focused to the middle of the droplet, and the spectra were integrated over about half a minute. Measurements on these samples served as a test during imaging runs to confirm that the calculated spectral dispersion imaged on the EMCCD had not drifted.

### SUPPLEMENTARY MATERIALS

[www.sciencesignaling.org/cgi/content/full/9/435/rs5/DC1](http://www.sciencesignaling.org/cgi/content/full/9/435/rs5/DC1)

Note S1. Details of FBI.

Note S2. Effect of anisotropy in  $n$  for calculated  $M'$ .

Note S3. Effect of uncertainty in  $n$  and  $\rho$  for calculated  $M'$ .

Note S4. Experimental determination of the refractive index and density of *Arabidopsis* ECMs.

Fig. S1. Schematic of the FBI setup.

Fig. S2. Sketch of the used microscope and spectrometer setup.

Fig. S3. FBI scans of epidermal onion cells.

Fig. S4. FBI scans of Lti6-tdTomato root cells.

Fig. S5. Width measurements of *Arabidopsis* hypocotyl longitudinal ECMs.

Fig. S6. Effect of plasmolysis on ECM and nearby cytoplasm.

Fig. S7. Determination of refractive index and density of *Arabidopsis* ECM by time-resolved fluorescence studies.

Fig. S8. Cross-sectional Brillouin imaging scans of cells in deep layers of *Arabidopsis* roots.

Fig. S9. Cross-sectional FBI scans of wild-type *Arabidopsis* root cells.

Reference (69)

### REFERENCES AND NOTES

1. R. O. Hynes, The extracellular matrix: Not just pretty fibrils. *Science* **326**, 1216–1219 (2009).
2. B. Trappmann, J. E. Gautrot, J. T. Connelly, D. G. T. Strange, Y. Li, M. L. Oyen, M. A. Cohen Stuart, H. Boehm, B. Li, V. Vogel, J. P. Spatz, F. M. Watt, W. T. S. Huck, Extracellular-matrix tethering regulates stem-cell fate. *Nat. Mater.* **11**, 642–649 (2012).
3. D. J. Cosgrove, Re-constructing our models of cellulose and primary cell wall assembly. *Curr. Opin. Plant Biol.* **22**, 122–131 (2014).
4. S. Wolf, H. Hofte, Growth control: A saga of cell walls, ROS, and peptide receptors. *Plant Cell* **26**, 1848–1856 (2014).

5. D. J. Cosgrove, Plant cell wall extensibility: Connecting plant cell growth with cell wall structure, mechanics, and the action of wall-modifying enzymes. *J. Exp. Bot.* **67**, 463–476 (2016).
6. K. L. Mui, C. S. Chen, R. K. Assoian, The mechanical regulation of integrin-cadherin crosslinking organizes cells, signaling and forces. *J. Cell Sci.* **129**, 1093–1100 (2016).
7. M. Miron-Mendoza, V. Koppaka, C. Zhou, W. M. Petroll, Techniques for assessing 3-D cell–matrix mechanical interactions in vitro and in vivo. *Exp. Cell Res.* **319**, 2470–2480 (2013).
8. A. Peaucelle, AFM-based mapping of the elastic properties of cell walls: At tissue, cellular, and subcellular resolutions. *J. Vis. Exp.* e51317 (2014).
9. A.-L. Routier-Kierzkowska, A. Weber, P. Kochova, D. Felekis, B. J. Nelson, C. Kuhlmeier, R. S. Smith, Cellular force microscopy for in vivo measurements of plant tissue mechanics. *Plant Physiol.* **158**, 1514–1522 (2012).
10. S. Yamada, D. Wirtz, S. C. Kuo, Mechanics of living cells measured by laser tracking microrheology. *Biophys. J.* **78**, 1736–1747 (2000).
11. S. A. Braybrook, Measuring the elasticity of plant cells with atomic force microscopy. *Methods Cell Biol.* **125**, 237–254 (2015).
12. A. Ikai, A review on: Atomic force microscopy applied to nano-mechanics of the cell. *Adv. Biochem. Eng. Biotechnol.* **119**, 47–61 (2010).
13. D. Wirtz, Particle-tracking microrheology of living cells: Principles and applications. *Annu. Rev. Biophys.* **38**, 301–326 (2009).
14. S. Rathgeber, H.-J. Beauvisage, H. Chevreau, N. Willenbacher, C. Oelschlaeger, Microrheology with fluorescence correlation spectroscopy. *Langmuir* **25**, 6368–6376 (2009).
15. T. Dehoux, M. Abi Ghanem, O. F. Zouani, M. Ducouso, N. Chigarev, C. Rossignol, N. Tsapis, M.-C. Durrieu, B. Audoin, Probing single-cell mechanics with picosecond ultrasonics. *Ultrasonics* **56**, 160–171 (2015).
16. S. Reiß, O. Stachs, R. Guthoff, H. Stolz, Non-invasive, spatially resolved determination of tissue properties of the crystalline lens with regard to rheology, refractive index, density and protein concentration by using Brillouin spectroscopy. *Klin. Monbl. Augenheilkd.* **228**, 1079–1085 (2011).
17. J. Randall, J. M. Vaughan, S. Cusak, Brillouin scattering in systems of biological significance [and discussion]. *Philos. Trans. R. Soc. London* **293**, 341–348 (1979).
18. G. Scarcelli, W. J. Polack, H. T. Nia, K. Patel, A. J. Grodzinsky, R. D. Kamm, S. H. Yun, Noncontact three-dimensional mapping of intracellular hydromechanical properties by Brillouin microscopy. *Nat. Methods* **12**, 1132–1134 (2015).
19. G. Scarcelli, S. H. Yun, Multistage VIPA etalons for high-extinction parallel Brillouin spectroscopy. *Opt. Express* **19**, 10913–10922 (2011).
20. G. Antonacci, M. R. Foreman, C. Paterson, P. Török, Spectral broadening in Brillouin imaging. *Appl. Phys. Lett.* **103**, 221105 (2013).
21. L. D. Landau, in *Theory of Elasticity*, L. P. Pitavskii, A. M. Kosevich, E. M. Lifshitz, Eds. (Butterworth-Heinemann, Oxford, ed. 3, 1986).
22. J. M. Vaughan, J. T. Randall, Brillouin scattering, density and elastic properties of the lens and cornea of the eye. *Nature* **284**, 489–491 (1980).
23. G. Antonacci, R. M. Pedrigo, A. Kondiboyina, V. V. Mehta, R. de Silva, C. Paterson, R. Krams, P. Török, Quantification of plaque stiffness by Brillouin microscopy in experimental thin cap fibroatheroma. *J. R. Soc. Interface* **12**, 20150843 (2015).
24. K. J. Koski, P. Akhenblit, K. McKiernan, J. L. Yarger, Non-invasive determination of the complete elastic moduli of spider silks. *Nat. Mater.* **12**, 262–267 (2013).
25. F. Palombo, C. P. Winlove, R. S. Edginton, E. Green, N. Stone, S. Caponi, M. Madami, D. Fioretto, Biomechanics of fibrous proteins of the extracellular matrix studied by Brillouin scattering. *J. R. Soc. Interface* **11**, 20140739 (2014).
26. S. Reiß, G. Burau, O. Stachs, R. Guthoff, H. Stolz, Spatially resolved Brillouin spectroscopy to determine the rheological properties of the eye lens. *Biomed. Opt. Express* **2**, 2144–2159 (2011).
27. S. Reiß, K. Sperlich, M. Hovakimyan, P. Martius, R. F. Guthoff, H. Stolz, O. Stachs, Ex vivo measurement of postmortem tissue changes in the crystalline lens by Brillouin spectroscopy and confocal reflectance microscopy. *IEEE Trans. Biomed. Eng.* **59**, 2348–2354 (2012).
28. G. Scarcelli, S. Besner, R. Pineda, S. H. Yun, Biomechanical characterization of keratocorneas ex vivo with Brillouin microscopy. *Invest. Ophthalmol. Vis. Sci.* **55**, 4490–4495 (2014).
29. G. Scarcelli, P. Kim, S. H. Yun, In vivo measurement of age-related stiffening in the crystalline lens by Brillouin optical microscopy. *Biophys. J.* **101**, 1539–1545 (2011).
30. G. Scarcelli, S. Kling, E. Quijano, R. Pineda, S. Marcos, S. H. Yun, Brillouin microscopy of collagen crosslinking: Noncontact depth-dependent analysis of corneal elastic modulus. *Invest. Ophthalmol. Vis. Sci.* **54**, 1418–1425 (2013).
31. G. Scarcelli, R. Pineda, S. H. Yun, Brillouin optical microscopy for corneal biomechanics. *Invest. Ophthalmol. Vis. Sci.* **53**, 185–190 (2012).
32. G. Scarcelli, S. H. Yun, In vivo Brillouin optical microscopy of the human eye. *Opt. Express* **20**, 9197–9202 (2012).
33. G. Scarcelli, S. H. Yun, Confocal Brillouin microscopy for three-dimensional mechanical imaging. *Nat. Photonics* **2**, 39–43 (2007).
34. K. Berghaus, J. Zhang, S. H. Yun, G. Scarcelli, High-finesse sub-GHz-resolution spectrometer employing VIPA etalons of different dispersion. *Opt. Lett.* **40**, 4436–4439 (2015).
35. T. Zhang, Y. Zheng, D. J. Cosgrove, Spatial organization of cellulose microfibrils and matrix polysaccharides in primary plant cell walls as imaged by multichannel atomic force microscopy. *Plant J.* **85**, 179–192 (2016).
36. S. A. Braybrook, H. Jönsson, Shifting foundations: The mechanical cell wall and development. *Curr. Opin. Plant Biol.* **29**, 115–120 (2016).
37. Y. Jaillais, T. Gaude, Sorting out the sorting functions of endosomes in Arabidopsis. *Plant Signal. Behav.* **2**, 556–558 (2007).
38. J. J. Petricka, C. M. Winter, P. N. Benfey, Control of Arabidopsis root development. *Annu. Rev. Plant Biol.* **63**, 563–590 (2012).
39. E. Gendreau, J. Traas, T. Desnos, O. Grandjean, M. Caboche, H. Hofte, Cellular basis of hypocotyl growth in Arabidopsis thaliana. *Plant Physiol.* **114**, 295–305 (1997).
40. E. M. Purcell, H. C. Torrey, R. V. Pound, Resonance absorption by nuclear magnetic moments in a solid. *Phys. Rev.* **69**, 37–38 (1946).
41. S. J. Strickler, R. A. Berg, Relationship between absorption intensity and fluorescence lifetime of molecules. *J. Chem. Phys.* **37**, 814–822 (1962).
42. K. Suhling, J. Siegel, D. Phillips, P. M. W. French, S. Lévêque-Fort, S. E. D. Webb, D. M. Davis, Imaging the environment of green fluorescent protein. *Biophys. J.* **83**, 3589–3595 (2002).
43. D. Toptygin, Effects of the solvent refractive index and its dispersion on the radiative decay rate and extinction coefficient of a fluorescent solute. *J. Fluoresc.* **13**, 201–219 (2003).
44. H. J. van Manen, P. Verkuijen, P. Wittendorp, V. Subramaniam, T. K. van den Berg, D. Roos, C. Otto, Refractive index sensing of green fluorescent proteins in living cells using fluorescence lifetime imaging microscopy. *Biophys. J.* **94**, L67–L69 (2008).
45. D. Magde, R. Wong, P. G. Seybold, Fluorescence quantum yields and their relation to lifetimes of rhodamine 6G and fluorescein in nine solvents: Improved absolute standards for quantum yields. *Photochem. Photobiol.* **75**, 327–334 (2002).
46. Y. Belkhadir, Y. Jaillais, P. Epple, E. Balsemão-Pires, J. L. Dangl, J. Chory, Brassinosteroids modulate the efficiency of plant immune responses to microbe-associated molecular patterns. *Proc. Natl. Acad. Sci. U.S.A.* **109**, 297–302 (2012).
47. Y. Jaillais, M. Hothorn, Y. Belkhadir, T. Dabi, Z. L. Nimchuk, E. M. Meyerowitz, J. Chory, Tyrosine phosphorylation controls brassinosteroid receptor activation by triggering membrane release of its kinase inhibitor. *Genes Dev.* **25**, 232–237 (2011).
48. N. Geldner, The endodermis. *Annu. Rev. Plant Biol.* **64**, 531–558 (2013).
49. A. Pfister, M. Barberon, J. Allassimone, L. Kalmbach, Y. Lee, J. E. Vermeer, M. Yamazaki, G. Li, C. Maurel, J. Takano, T. Kamiya, D. E. Salt, D. Roppolo, N. Geldner, A receptor-like kinase mutant with absent endodermal diffusion barrier displays selective nutrient homeostasis defects. *Elife* **3**, e03115 (2014).
50. M. Chen, J. Chory, Phytochrome signaling mechanisms and the control of plant development. *Trends Cell Biol.* **21**, 664–671 (2011).
51. L. Li, K. Ljung, G. Breton, R. J. Schmitz, J. Pruneda-Paz, C. Cowing-Zitron, B. J. Cole, L. J. Ivans, U. V. Pedmale, H.-S. Jung, J. R. Ecker, S. A. Kay, J. Chory, Linking photoreceptor excitation to changes in plant architecture. *Genes Dev.* **26**, 785–790 (2012).
52. E. F. Crowell, H. Timpano, T. Desprez, T. Franssen-Verheijen, A.-M. Emons, H. Höfte, S. Vernhettes, Differential regulation of cellulose orientation at the inner and outer face of epidermal cells in the Arabidopsis hypocotyl. *Plant Cell* **23**, 2592–2605 (2011).
53. G. Refrégier, S. Pelletier, D. Jaillard, H. Höfte, Interaction between wall deposition and cell elongation in dark-grown hypocotyl cells in Arabidopsis. *Plant Physiol.* **135**, 959–968 (2004).
54. T. Desprez, S. Vernhettes, M. Fagard, G. Refrégier, T. Desnos, E. Aletti, N. Py, S. Pelletier, H. Höfte, Resistance against herbicide isoxaben and cellulose deficiency caused by distinct mutations in same cellulose synthase isoform CESA6. *Plant Physiol.* **128**, 482–490 (2002).
55. K. Kim, H. Yi, M. S. Zamil, M. A. Haque, V. M. Puri, Multiscale stress–strain characterization of onion outer epidermal tissue in wet and dry states. *Am. J. Bot.* **102**, 12–20 (2015).
56. B. Audoin, C. Rossignol, N. Chigarev, M. Ducouso, G. Forget, F. Guillemot, M. C. Durrieu, Picosecond acoustics in vegetal cells: Non-invasive in vitro measurements at a sub-cell scale. *Ultrasonics* **50**, 202–207 (2010).
57. L. Beauzamy, M. Louveaux, O. Hamant, A. Boudaoud, Mechanically, the shoot apical meristem of Arabidopsis behaves like a shell inflated by a pressure of about 1 MPa. *Front. Plant Sci.* **6**, 1038 (2015).
58. F. Corson, O. Hamant, S. Bohn, J. Traas, A. Boudaoud, Y. Couder, Turning a plant tissue into a living cell froth through isotropic growth. *Proc. Natl. Acad. Sci. U.S.A.* **106**, 8453–8458 (2009).
59. T. Hamann, M. Bennett, J. Mansfield, C. Somerville, Identification of cell-wall stress as a hexose-dependent and osmosensitive regulator of plant responses. *Plant J.* **57**, 1015–1026 (2009).
60. O. Hamant, J. Traas, The mechanics behind plant development. *New Phytol.* **185**, 369–385 (2010).
61. F. Boudon, J. Chopard, O. Ali, B. Gilles, O. Hamant, A. Boudaoud, J. Traas, C. Godin, A computational framework for 3D mechanical modeling of plant morphogenesis with cellular resolution. *PLOS Comput. Biol.* **11**, e1003950 (2015).

62. E. F. Crowell, M. Gonneau, S. Vernhettes, H. Höfte, Regulation of anisotropic cell expansion in higher plants. *C. R. Biol.* **333**, 320–324 (2010).
63. M. Uyttewaal, J. Traas, O. Hamant, Integrating physical stress, growth, and development. *Curr. Opin. Plant Biol.* **13**, 46–52 (2010).
64. A. Peaucelle, R. Wightman, H. Höfte, The control of growth symmetry breaking in the *Arabidopsis* hypocotyl. *Curr. Biol.* **25**, 1746–1752 (2015).
65. A. Caño-Delgado, S. Penfield, C. Smith, M. Catley, M. Bevan, Reduced cellulose synthesis invokes lignification and defense responses in *Arabidopsis thaliana*. *Plant J.* **34**, 351–362 (2003).
66. D. Richardson, The use of echelles in spectroscopy. *Spectrochim. Acta* **6**, E61–E65 (1953).
67. X. Shijun, A. M. Weiner, C. Lin, A dispersion law for virtually imaged phased-array spectral dispersers based on paraxial wave theory. *IEEE J. Quantum Elect.* **40**, 420–426 (2004).
68. D. Y. Liu, B. T. Kuhlmey, P. M. C. Smith, D. A. Day, C. R. Faulkner, R. L. Overall, Reflection across plant cell boundaries in confocal laser scanning microscopy. *J. Microsc.* **231**, 349–357 (2008).
69. K. R. K. Iyer, P. Neelakantan, T. Radhakrishnan, Birefringence of native cellulosic fibers. I. Untreated cotton and ramie. *J. Polym. Sci.* **6**, 1747–1758 (1968).

**Acknowledgments:** We thank R. Latham and M. Zimmer (Institute of Molecular Pathology, Vienna, Austria) for preparing calibration samples and M. Platre for help in raising the *35S::Lti6-tdTomato* lines. We are grateful to A. Aszodi and A. Gyenesei [Bioinformatics and Scientific Computing Facility, Vienna Biocenter Core Facility (VBCF)] for expert guid-

ance on the statistical analysis. We also thank the VBCF Plant Sciences facilities for the use of the plant growth chambers. We would also like to thank N. Geldner for sharing the *CASP1::mCherrySYP122 Arabidopsis* transgenic line. We also thank J. M. Watson for providing constructive comments on our article. Finally, we thank N. Daubel for technical advices. **Funding:** K.E., E.R.S.G., and L.Z. acknowledge funding from the Austrian Federal Ministry of Science, Research & Economy, and the City of Vienna through the VBCF. This work was supported by grants from the Austrian Academy of Science through the Gregor Mendel Institute (Y.B. and T.G.). This work was also supported by Austrian Science Fund (FWF) grant P25594-168 B21 and a Heisenberg Fellowship from the German Research Foundation (DFG, GR 2104/4-1) to T.G. **Author contributions:** K.E., T.G., J.K., and Y.B. conceived and designed the experiments. K.E., E.R.S.G., and L.Z. constructed the FBI setup. J.K., M.G., S.W., and K.E. performed the experiments. K.E., M.G., and J.K. analyzed the data. Y.J. provided reagents. K.E. and Y.B. wrote the manuscript with input from the other authors. **Competing interests:** The authors declare that they have no competing interests. **Data and materials availability:** Custom MATLAB scripts are available upon request or from the Web site: [www.vbcf.ac.at/advmicro](http://www.vbcf.ac.at/advmicro).

Submitted 8 March 2016

Accepted 17 June 2016

Final Publication 5 July 2016

10.1126/scisignal.aaf6326

**Citation:** K. E. Elsayad, S. Werner, M. Gallemí, J. Kong, E. R. Sánchez Guajardo, L. Zhang, Y. Jaillais, T. Greb, Y. Belkhadir, Mapping the subcellular mechanical properties of live cells in tissues with fluorescence emission–Brillouin imaging. *Sci. Signal.* **9**, rs5 (2016).

## Mapping the subcellular mechanical properties of live cells in tissues with fluorescence emission–Brillouin imaging

Kareem Elsayad, Stephanie Werner, Marçal Gallemí, Jixiang Kong, Edmundo R. Sánchez Guajardo, Lijuan Zhang, Yvon Jaillais, Thomas Greb and Youssef Belkhadir

*Sci. Signal.* **9** (435), rs5.  
DOI: 10.1126/scisignal.aaf6326

### Seeing mechanical properties of living cells

Mechanical properties of cells and the matrix that surrounds them contribute to cell shape, control cell migration, and regulate cell growth. Elsayad *et al.* engineered a microscope system that integrated fluorescence emission detection with detection of a light-scattering process called the Brillouin frequency shift and called the method fluorescence emission–Brillouin scattering imaging (FBI). With this optical approach, the authors showed that the mechanical properties of live plants can be visualized at the submicrometer scale and demonstrated that this approach can be used to investigate regulatory events that alter cellular and extracellular mechanical properties of living cells within tissues. This work also revealed that the cytoplasm near the cell membrane and the extracellular matrix are regions of locally increased stiffness and showed that the sides parallel to the growth axis of an expanding plant hypocotyl, but not root, cells are "stiffer" than the sides perpendicular to the growth axis. Thus, FBI is another tool in the microscopy toolkit for exploring properties of cells and tissues.

#### ARTICLE TOOLS

<http://stke.sciencemag.org/content/9/435/rs5>

#### SUPPLEMENTARY MATERIALS

<http://stke.sciencemag.org/content/suppl/2016/06/30/9.435.rs5.DC1>

#### RELATED CONTENT

<http://stke.sciencemag.org/content/sigtrans/2/84/ra45.full>  
<http://stke.sciencemag.org/content/sigtrans/6/305/ec300.abstract>  
<http://stke.sciencemag.org/content/sigtrans/2002/118/pe5.full>  
<http://stke.sciencemag.org/content/sigtrans/9/440/ec183.abstract>  
<http://stke.sciencemag.org/content/sigtrans/9/446/eg9.full>  
<http://stke.sciencemag.org/content/sigtrans/9/452/ra106.full>  
<http://stke.sciencemag.org/content/sigtrans/10/478/eaan5821.full>  
<http://stke.sciencemag.org/content/sigtrans/10/481/eaal3154.full>  
<http://science.sciencemag.org/content/sci/353/6299/587.full>

#### REFERENCES

This article cites 67 articles, 18 of which you can access for free  
<http://stke.sciencemag.org/content/9/435/rs5#BIBL>

#### PERMISSIONS

<http://www.sciencemag.org/help/reprints-and-permissions>

Use of this article is subject to the [Terms of Service](#)